ap

Asian Journal of Physics
Vol. 25, No 3 (2016) 363-386
Available on: www.asianjournalofphysics.in

Solar origins of space weather

Kiran Jain and Rudolf W Komm
National Solar Observatory, 950 N. Cherry Avenue, Tucson, AZ 85719, USA

Space weather refers to the varying conditions in the space environment near Earth that are driven by the Sun and its changing magnetic field. The magnetic field originates in the interior of the Sun and extends through-out the solar atmosphere. We discuss the solar sources of space weather and focus on coronal mass ejections (CMEs), flares, and solar energetic particles (SEP) and on the on-going efforts to predict these eruptive events and their effect on space weather.

Keywords: Sun: activity; Sun: active regions; Sun: flares; Sun: coronal mass ejections; Sun: UV radiation; Space weather

1 Introduction

Space weather commonly refers to the varying conditions in the space environment especially near Earth that are driven by the Sun and its magnetic field. The effect of space weather ranges from beautiful polar lights to the degradation of the performance and reliability of ground- and space-based technological systems. The great solar-terrestrial disturbance of September 1859 (Carrington event, Fig 1, [1]) caused auroras so brilliant that newspapers could be read by their light and disturbed telegraph systems in Europe and the U.S. with spark discharges (caused by ground-induced currents) shocking telegraph operators and setting the telegraph paper on fire [2, 3]. The discovery that a geomagnetic storm occurred within a day after the flashes of light observed by Carrington can be considered the beginning of space weather research [4]. (Since the 1980s, it is known that geomagnetic activity is caused by coronal mass ejections and not by flares.) This event from 1859 is near the top of the list of several measures of solar-induced disturbances caused by solar eruptive events during the last 150 years [5].

More recently, the "Halloween events" that occurred during several days in late October to early November 2003 produced powerful X-ray flares and coronal mass ejections (CMEs) that were pointed toward the Earth and caused major geomagnetic storms [6, 7]. Figure 2 shows examples of the aurora produced by the geomagnetic storm during this period. The realization that modern technology is vulnerable to space weather effects is not new. Early in the 20th century, it was noticed that solar activity affects the Earth's ionosphere and thus the propagation of radio waves used for communications [8]. However, technology depending on ground-based electrical systems and space-based assets is increasingly vulnerable to space weather events.

The Sun produces a variety of eruptive events that affect the space-weather near Earth. The origin of solar eruptive events lies in the complex magnetic field that emerges from the solar interior and extends throughout the solar atmosphere. The solar phenomena that cause and shape space weather in the Earth environment are flares, CMEs, solar energetic particles (SEPs), and the solar wind. Flares release a large amount of energy in the form of radiation and heating and acceleration of particles. Their soft X-ray radiation indicates the sudden heating of the corona to temperatures of several 10^7 K [9]. The intensity in soft X-rays has been used for flare classification (*http://www.swpc.noaa.gov/products/goes-x-ray-flux*). CMEs consist

Corresponding author :
e-mail: kjain@nso.edu (Kiran Jain)

of large structures containing plasma and magnetic fields that are expelled from the Sun on time scales of minutes and hours. CMEs inject large quantities of mass and magnetic flux into the heliosphere, causing major transient disturbances [10]. They can drive interplanetary shocks, a key source of SEPs, which then drive large-scale density waves out into space. Flare and CME eruptions might be different parts of the same underlying magnetic process. However, most occur independently of each other [11, 12]. Flares and shock waves in the corona and interplanetary space accelerate ions and electrons (SEPs). SEPs can reach up to about half the speed of light and arrive at Earth only minutes after the eruptive event, while it takes about 1 to 4 days for distortions in the magnetic field due to CMEs to reach Earth. This makes SEP events particularly dangerous for astronauts outside the Earth's magnetosphere. All these disturbances propagate through the solar wind, a mixture of ions and electrons flowing away from the Sun. The solar wind interacts with the Earth's magnetic field and shapes its magnetosphere [4].

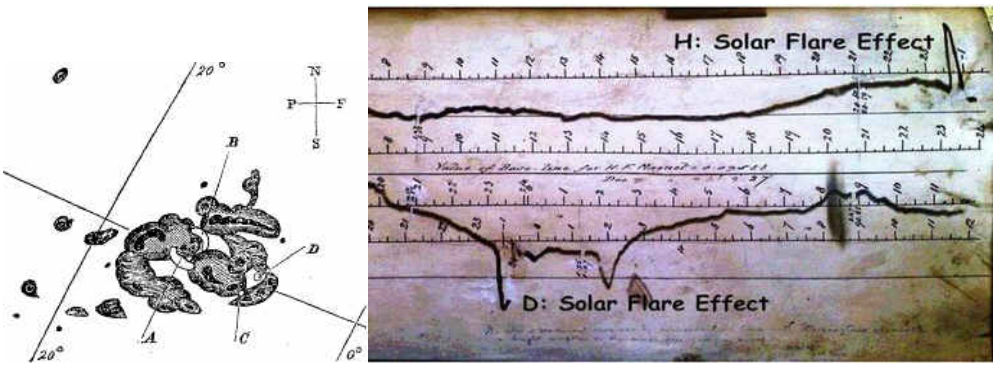

Fig 1. (left) Sunspots sketched by Richard Carrington on Sept 1, 1859. Regions marked with A and B were believed to be the initial locations of flares and then a few minutes later, more flares were erupted from C and D. Courtesy: Royal Astronomical Society; (right) A magnetogram recorded at the Greenwich Observatory in London during the Carrington Event of 1859. The lower line (D) represents compass direction; the upper line (H) represents horizontal force. Courtesy: British Geological Survey

The most significant impacts of space weather on technology fall into three categories: (a) geomagnetic disturbances that induce electric currents which disturb the electric power infrastructure, (b) variability in the ionospheric electron density that impacts positioning and navigation systems (GPS), and (c) energetic particles that affect spacecrafts, astronauts, and air traffic (see [13] for a review of the terrestrial perspective of space weather). For example, solar CMEs can cause magnetic reconnection at the day-side Earth magnetosphere when the CMEs are Earth-directed with a strong magnetic field that is oppositely directed to the Earth's magnetic field. The coupling to the Earth magnetosphere produces geomagnetically induced currents (GIC). Strong GICs can cause the saturation of power transformers; the resulting heat has to be dissipated and can damage the transformers. Solar CMEs and flares can affect the Earth's ionosphere causing spatial gradients and temporal variations that affect positioning and navigation. Space weather is the largest contributor to single-frequency GPS errors and a significant factor for differential GPS [14]. The EUV radiation produced during the flaring process causes the heating and expansion of the Earth's atmosphere, which increases the drag and lowers the orbit of satellites in low-Earth orbits [15]. SEPs are not only a radiation risk for satellites and astronauts, but can also lead to increased radiation dosage for airplane crews and passengers especially along polar routes. Scientists and users of space-weather forecasts discuss how to better understand space weather and deal with its consequences at annual workshops, such as the Space Weather Workshop held every April in Colorado, US (*http://www.swpc.noaa.gov/content/ annual-meeting*) and the European Space Weather Week held in November in Belgium *(http://www.stce.be/esww13*).

Recently, a space-weather roadmap has been published by the Committee on Space Research (COSPAR) and the International Living With a Star (ILWS). The roadmap assesses how to advance the science with the aim of better meeting the users' needs [16].

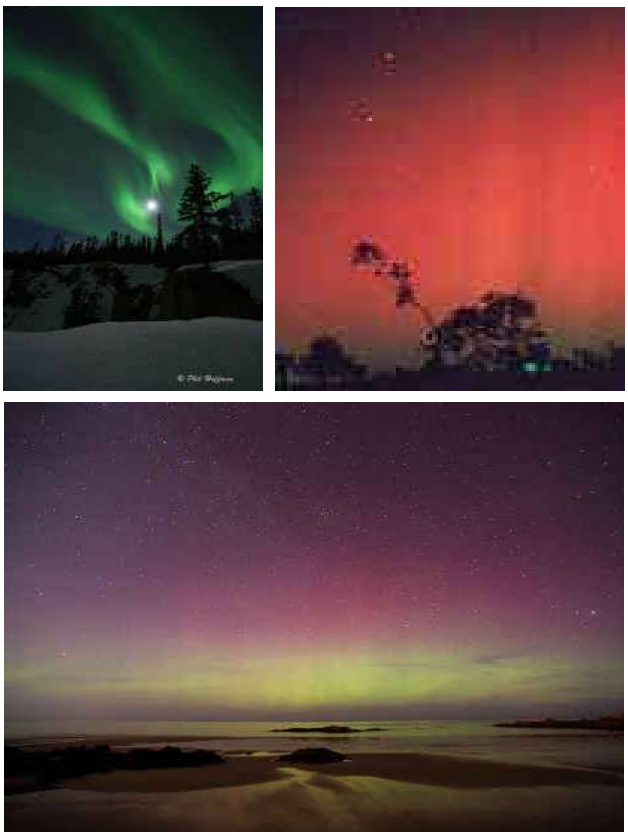

Fig 2. Auroras produced by geomagnetic storm in October 2003. (Source: *www.spaceweather.com*)

The space weather effort consists of three steps: (a) synoptic observations of the Sun, (b) the prediction of solar activity, and (c) the forecasting of space weather. First, the Sun has to be continuously monitored with sufficient temporal cadence and spatial resolution (see reviews by Gosain [17] and Pesnell [18] in this volume). This can be done with space-based observatories, such as ACE (*http://www.srl.caltech.edu/ACE/ace_mission.html*), STEREO (*http://stereo.gsfc.nasa.gov*, [19]), and the Solar Dynamics Observatory (SDO) spacecraft (*http://sdo.gsfc.nasa.gov*, [20]) and with ground-based networks [21], such as the Global Oscillation Network Group (GONG, *http://gong.nso.edu/data*) and the Global High-Resolution Hα Network (GHN, *swrl.njit.edu/ghn*_web). A new ground-based synoptic network (Solar Physics Research Integrated Network Group or SPRING) is being planned [22]. Then, the solar observations have to be fed into models, such as the Wang-Sheeley-Arge (WSA) Enlil model. The semi-empirical near-Sun WSA model approximates the outflow at the base of the solar wind [23] using GONG magnetograms and the magnetohydrodynamic numerical model (Enlil) simulates the resulting flow evolution out to Earth [24, 25]. This model has been transitioned into operational at the National Weather Service's (NWS) Space Weather Prediction Center (SWPC; *http://www.swpc.noaa.gov*) [26]. The successful transition from research to operations (R2O) is crucial for the forecasting of space weather events [27]. In the following sections, we discuss the physics of CMEs, flares, and SEPS and the on-going efforts to predict these eruptive events and their effect on space weather.

2 Solar origins of space weather and their impact

There are several solar phenomena that can affect the space weather. Active regions (ARs) are primarily responsible for extreme space weather, however all regions do not influence it in the same way. Major drivers are the solar storms that occur when a large-scale magnetic eruption, often causing a coronal mass ejection and associated solar flare from the regions of high magnetic field, accelerates charged particles in the solar atmosphere to very high velocities. Figure 3 provides a comprehensive view of the drivers of space weather. A description of various solar phenomena can be found in various reviews and books (e.g., see review by Ambastha in this issue [28]). However, we describe them here in the context of space weather and how these solar events impact the space weather.

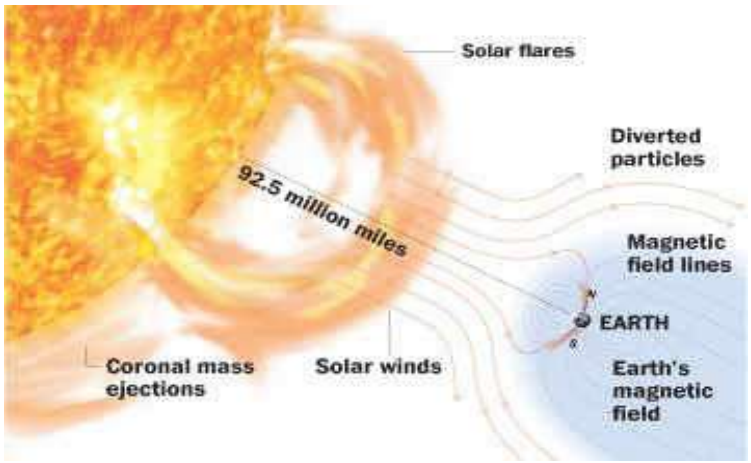

Fig 3. Solar drivers of the space weather. Credit: NOAA/SWPC

2.1 Active regions and their complexity

Solar active regions are generally formed with the evolution of sunspot groups, hence harbor strong magnetic fields (e.g., see review by van Driel-Gesztelyi [29]). Some groups have a more complex magnetic structure than other groups and are more likely to produce solar flares and other energetic events. Thus, the active regions can be classified on the basis of their magnetic configuration (known as the Mt Wilson classification [30]). Bigger sunspots are often more complex and get a β, βγ or βγδ configuration in the Mt Wilson classification. Observations show that the regions with δ configuration are very active and produce the most intense solar flares.

It is believed that the active regions emerge preferentially in locations where other such emergence has occurred before. Most of the magnetic flux is organized in so-called activity complexes [31-33]. These locations of recurrent flux emergence in or close to pre-existing active regions last for typically five to seven solar rotations. The emergence of new magnetic flux in pre-existing magnetic regions causes an increase in topological complexity of the magnetic field [34], which leads to favorable conditions for flares and CMEs [32, 35, 36-38]. Highly non-potential magnetic fields are very probably responsible for strong eruptive phenomena such as flares and CMEs. It is not only the size of an active region that matters for its potential to produce eruptive events; its magnetic complexity is even more important. For example, active region 12192 appeared in October 2014 and was about the same size or even bigger than active region 10486 that appeared nearly 11 years before and generated the Halloween events (see Fig 4). However, region 12192 failed to produce any CMEs [39].

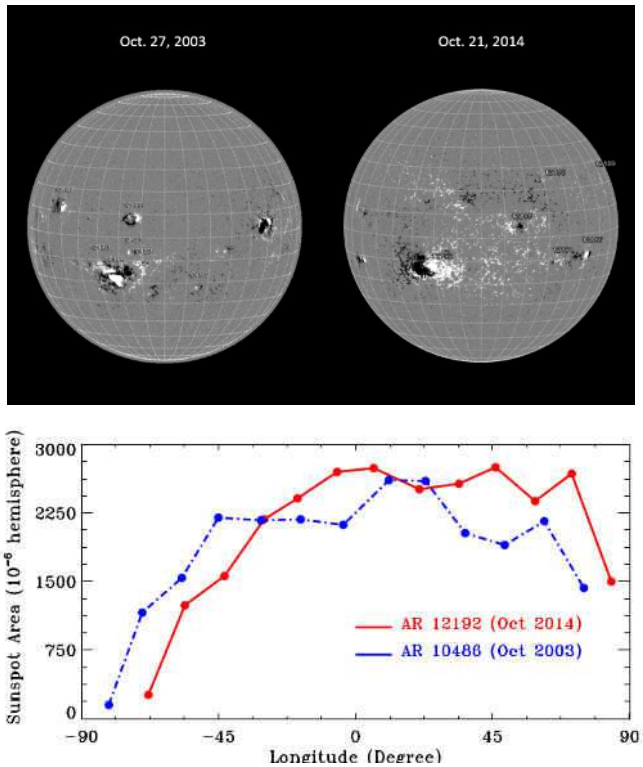

Fig 4. (Top) Magentograms showing two big active regions that emerged in cycle 23 and 24: (left) SOHO/MDI magnetogram showing AR 10486, and (right) SDO/HMI magnetogram showing AR12192. (Bottom) Comparison of the size of both active regions as they cross the visible side of the Sun.

The characteristics of sunspots within the active regions are important to define their complexity. While some move on the solar disk with solar rotation, while other sunspots rotate around their umbral centers or other sunspots within the same active region. The sunspots in this category are generally known as rotating sunspots [40, 41]. It is seen that there is no preferential direction for their rotation, some rotate in clockwise direction while others in anti-clockwise direction. Studies suggest that this kind of rotation may lead to the buildup of energy, which might be later released by a flare [42]. The relationship between the rotating sunspots and flares have been studied in detail by several workers [43, 44, and references therein] and also found them to have higher probability for flares. It is also suggested that the regions with sunspots of rotating direction opposite to the differential rotation have much higher strong flare productivity.

It is known from observations that magnetic flux tubes emerge pre-twisted from the solar interior into the corona. A quantitative measure of topological complexity is the magnetic helicity, which measures twisting and linking of the magnetic field [45, 46]. Two commonly used magnetic helicity proxies are the current helicity density [47, 48] and the mean twist parameter, [49, 50]. These can be derived from full-disk vector magnetograms from instruments, such as the Vector Spectromagnetograph (VSM) instrument of the Synoptic Optical Long-term Investigations of the Sun (SOLIS) synoptic facility and the Helioseismic and Magnetic Imager (HMI) instrument onboard SDO. The kinetic helicity [51] can be used as a proxy for magnetic helicity in the solar interior, where the magnetic fields originate. Theoretical expectations are that right-handed eddies lead to right-handed magnetic twist.

2.2 Solar flares

Solar flares are large outbursts of electromagnetic radiation from the Sun typically lasting from minutes to hours that may cover a wide range of electromagnetic waves such as radio, visible light, X-rays, and gamma rays (e.g., see review by Benz [52]). Emissions in these wavelengths come from the atmospheric layers extending from the chromosphere to the corona. In extreme cases, even the photosphere responds to big flares, observed as white-light brightening. The key physical processes for producing a flare are: the emergence of magnetic field from the solar interior to the solar atmosphere (flux emergence), local enhancement of electric current in the corona (formation of a current sheet), and rapid dissipation of electric current (magnetic reconnection) that causes shock heating, mass ejection, and particle acceleration [9]. In the pre-flare phase, the coronal plasma in the flare region slowly heats up and is visible in soft X-rays and EUV. A large number of energetic electrons (up to 10^{38}) and ions (with similar total energy) is accelerated in the impulsive phase, when most of the energy is released. The total energy released during flares can differ by several orders of magnitude from 10^{9} Joules for small events up to some 10^{25} Joules for most energetic events. A major portion of energy goes into the radiation while the rest goes in the heating and accelerating charged particles depending on the type of flares.

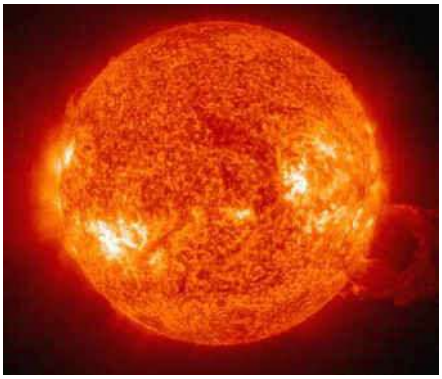

Fig 5. Solar flare in H-alpha.

The flares are generally observed using filters to isolate the light emitted by hydrogen atoms in the red region of the solar spectrum, i.e. the H-α spectral line (see Fig 5). In EUV, these are visible as bright flashes. There are several flare patrol programs at various observatories around the world however various space missions such as RHESSI, Yohkoh, TRACE, SOHO, SDO have added another dimension to the flare database that allows us to understand the flare mechanisms in great detail. In addition, NOAA has been regularly providing flare intensity in the 1 minute averages of 0.1 – 0.8 nm spectral band using GOES XRS instrument. This intensity on the logarithmic scale is being used to classify flares in five categories: X, M, C, B and A class with X being the largest. The X-ray flux as measured by GOES during a series of flaring events in 2003 around Halloween is shown in Fig 6.

Big flares can impact the Earth's atmosphere with radiation that may interfere with radio, GPS systems, and power grids. X-rays and EUV light from solar flares ionize the Earth's atmosphere, causing an enhancement of the lower part of the Sun-facing ionosphere which blocks radio signals that normally are reflected off of the ionosphere [13]. The reflected radio waves off the ionosphere permit long distance radio communication in the absence of clear line-of-sight between the transmitter and receiver. When the radio waves are absorbed due to the significantly enhanced ionosphere, radio communication gets disrupted and create conditions known as "radio blackouts". It is basically the absence of a capability to communicate on high frequency bands (in the 5–35 MegaHz spectral range), but lower frequency radio communications may also be degraded during big flares.

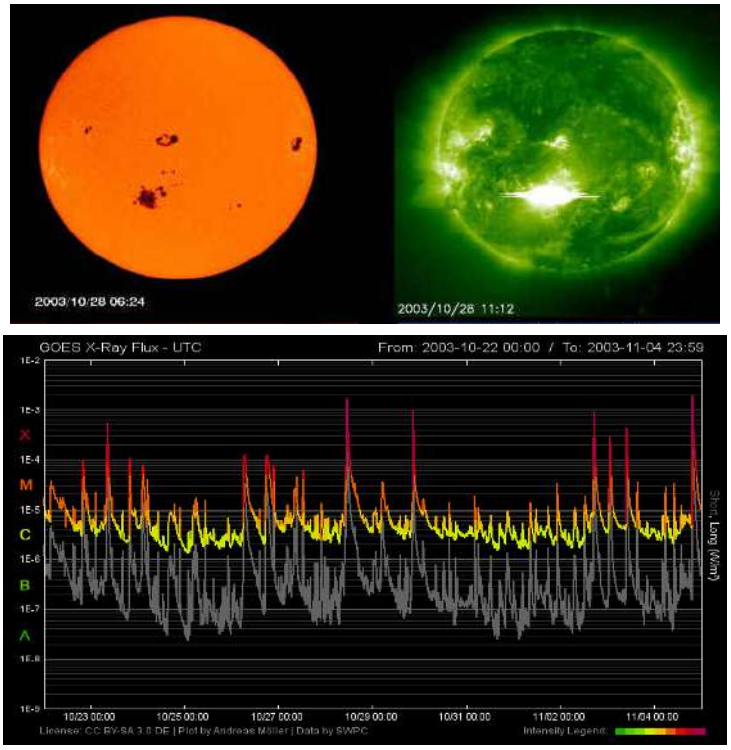

Fig 6. (Top) On the left is the visible light image of the solar disk showing the sunspot group that produced the X 17-class flare and the same region in an EIT image during flare (bright region in the southern hemisphere) Credit: SOHO/NASA/ESA. (Bottom) GOES X-ray flux measured during Halloween events (Courtesy: *http://www.polarlicht-vorhersage.de/goes_archive*).

2.3 CMEs

Coronal mass ejections are large explosions of magnetic field and plasma from the Sun's corona (Fig 7). These originate from highly twisted magnetic field structures on the Sun. The CMEs can erupt either from the cool plasmas trapped in the flux ropes in the corona, often referred to as filaments or prominences, or from the active regions on the Sun, often accompanied by large solar flares, see review by Low [53]. CMEs travel outward from the Sun typically at speeds of about 300 km/s, but can be as slow as 100 km/s or faster than 3000 km/s. The fastest CMEs erupt from large active regions harboring the strongest magnetic field concentrations on the Sun [54]. While fast CMEs can reach Earth in as little as 14–17 hours, slower CMEs from the quiet region filament eruptions take several days to travel the distance from the Sun to Earth. Because CMEs have an embedded magnetic field that is stronger than the background field of the solar wind, they expand in size as they propagate outward from the Sun forming the magnetic cloud. Because of their large size, slower CMEs may take as long as 24 to 36 hours to pass over the Earth after the arrival of the leading edge. Determining the geo-effectiveness of CMEs has been a topic of immense interest in space weather studies and has been discussed in a large number of papers (see review by Lavraud and Rouillard [55], and references therein).

Images of CMEs are taken near the Sun primarily by coronagraphs onboard spacecrafts. Coronagraphs view the outward flow of density structures emanating from the Sun by observing Thomson-scattered sunlight from the free electrons in coronal and heliospheric plasma. Determination of the size, speed, direction, and density of CMEs are important parameters to determine their geo-effectiveness and

have been widely studied (e.g., [56-58] and references therein). These properties can be estimated by using the observations from ground-based and space-based multi-instrument data sets. Since the launch of SOHO in 1995, multiple coronagraphs of Large Angle Spectrometric Coronagraphs (LASCO) have been imaging the corona continuously from 1.1 to 30 R_{sun}. Till now, LASCO has detected several thousand CMEs ([59], *http://cdaw.gsfc.nasa.gov/CME list/*). In order to capture a better view of the CMEs, twin Solar Terrestrial Relations Observatory (STEREO) spacecrafts were launched in 2006 to provide simultaneous images of the corona from two vantage points, i.e., from ahead and behind spacecraft (*http://stereo.gsfc.nasa.gov/*). These are useful to study the 3-D structure of CMEs. Disk observations of the solar atmosphere from STEREO are made in extreme ultraviolet wavelengths and the coronal observations are in white light. Using STEREO pair images, one can also determine the true speeds and directions of the leading edge of CMEs. These are extremely valuable for space weather predictions, as one can not only estimate the true speed and propagation direction of a CME in the corona, but also the exact arrival time at the Earth. Unfortunately, communication with the STEREO Behind spacecraft was interrupted in October 2014 immediately after a planned reset of the spacecraft and no further communications have been successful till now. However, these observations have played an important role in advancing the space weather studies and improving the forecast capabilities. CMEs traveling faster than the fast mode wave speed of solar wind plasma (the space equivalent of the Earths sound speed) generate shock waves [60]. These shock waves accelerate charged particles ahead of them create a much of the solar radiation storm affiliated with large-scale solar eruptions. Often, the first signal of CME hitting the Earth environment is the plasma density jump due to the shock waves passage. When CMEs impact the Earths magnetosphere, geomagnetic storms and enhanced aurora are produced (as shown in Fig 2, the examples of aurora produced during the October 2003 period).

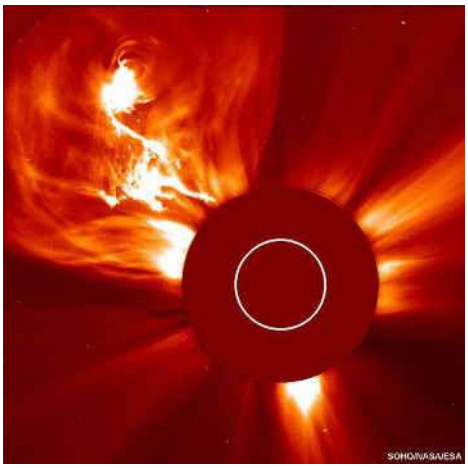

Fig 7. LASCO coronagraph image showing the eruption of a large CME. Credit: SOHO/NASA/ESA.

Geomagnetic storms are defined as the temporary disturbances of the Earth's magnetosphere and quantified by changes in the Dst (disturbance storm time) index. The Dst index estimates the globally averaged change of the horizontal component of the Earth's magnetic field at the magnetic equator based on measurements. It is computed once per hour and reported in near-real-time. During quiet times, Dst is between +20 and –20 nano-Tesla (nT). The size of a geomagnetic storm is classified as moderate (–100 nT < Dst < –50 nT), intense (–200 nT < Dst < –100 nT) or super-intense (minimum of Dst < –200 nT) [61]. In order to predict the strength of the resulting geomagnetic storm, estimates of the magnetic field strength and direction are important.

As mentioned above, fast CMEs are the sources of high energetic particles [62, 63]. Such fast CMEs

can give rise to intense geomagnetic storms on arrival at the Earth. Although the increase in the number of energetic particles takes place within a few hours of the onset of a CME, the geomagnetic storm generally occurs 1 to 4 days later. It is believed that the initial phase of the resulting geomagnetic storm is triggered by an increase in the plasma pressure accompanied by an increase in the density and speed of the solar wind at and behind the interplanetary shock. The main phase is governed, on the other hand, by the southward component of the interplanetary magnetic field. In addition, halo CMEs originating from regions close to the center of the Sun are likely to be geo-effective [64, 65].

2.4 Coronal holes and solar wind

Coronal holes are the darkest regions seen on the Sun that can be observed both on the solar disk and above the solar limb [66]. Coronal holes have a different appearance at different wavelengths of the solar spectrum. They are most easily identified in EUV and X-ray images of the Sun, where they appear as dark regions (see Fig 8) while in infrared, coronal holes appear brighter than the surrounding areas. These are associated with rapidly expanding open magnetic fields and the acceleration of the high-speed solar wind. The solar wind consists mainly of protons and electrons in a state known as a plasma with embedded magnetic field flows continuously outward from the Sun. Different regions on the Sun produce solar wind of different speeds and densities [67, 68]. Polar coronal holes produce solar wind of high speed up to 800 km/s [69]. Since both poles of the Sun have large, persistent coronal holes, high latitudes are filled with fast solar wind. In the equatorial plane, the most common state of the solar wind is the slow one with speeds of about 400 km/s. This portion of the solar wind forms the equatorial current sheet that can be nearly flat during the quiet periods.

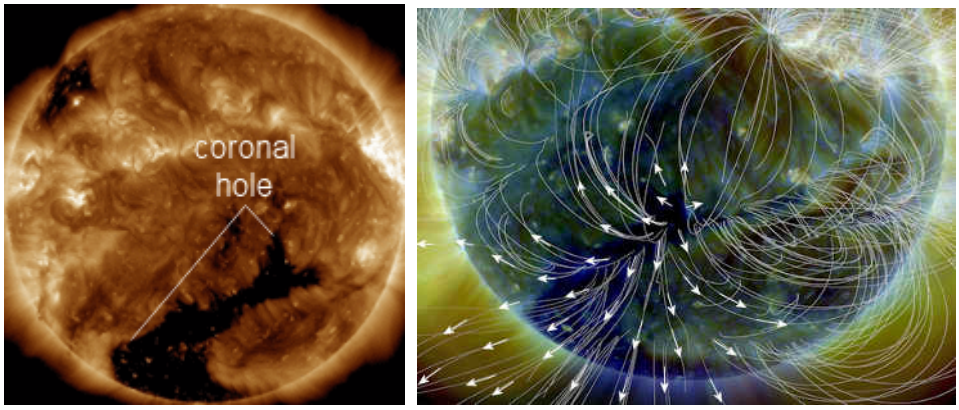

Fig 8. (Left) Coronal holes observed at 193 Å in transition region/corona on Feb 16, 2016. (Right) Predicted solar wind flow from the coronal holes are shown by white arrows. Credit: SDO/AIA.

With the increase in solar activity, the active regions, coronal holes, and other complex structures are abundant on the solar surface that modify the solar wind and current sheet. Because the Sun rotates every 27 days, the solar wind becomes a complex spiral of high and low speeds and high and low densities. When high speed solar wind overtakes slow wind, it creates a region known as the corotating interaction region with very high density solar wind and strong magnetic fields. Above the current sheet, the higher speed solar wind typically has a dominant magnetic polarity in one direction and below the current sheet, the polarity is in the opposite direction. As the Earth moves through this evolving ballerina skirt, it is sometimes within the heliospheric current sheet, sometimes above it and sometime below it. The location of the Earth with respect to the current sheet is important because space weather impacts are highly dependent on the solar wind speed, the solar wind density, and the direction of the magnetic field embedded in the solar wind.

Solar wind has a direct impact on space weather. High speed winds produce geomagnetic storms

while slow solar wind produces calm space weather. Thus, specifying and forecasting the solar wind is critical for accurate forecasts of space weather and its impacts at Earth. NASA's Advanced Composition Explorer (ACE) mission has been observing particles of solar, interplanetary, interstellar, and galactic origins, spanning the energy range from solar wind ions to galactic cosmic ray nuclei for about two decades [70]. From a vantage point approximately 1/100 of the distance from the Earth to the Sun at L1, ACE measures over a wide range of energy and nuclear mass, under all solar wind flow conditions and during both large and small particle events including solar flares. Observations from ACE provide near-real-time solar wind information (approximately 45-60 minutes in advance of its arrival at Earth). An advance warning of geomagnetic storms is important to avoid catastrophic effects, such as overloaded power grids, disruption in communications on Earth, and the hazard to astronauts. This mission was launched in 1997 and is expected to last until 2024.*2.5 Solar irradiance*

Solar Extreme Ultraviolet (EUV) is solar radiation that covers the wavelengths 10 – 120 nm of the electromagnetic spectrum (see Fig 9). It varies on different time scales, changes by a factor of ten over the course of a typical solar cycle, in contrast to the total solar irradiance (TSI) that only changes by a factor of 0.1% (see review by Fröhlich and Lean [72]). It also varies as much as an order of magnitude on time scales of minutes to hours, typical for solar flares. During the passage of big active regions, TSI drops due to the sunspot darkening. UV irradiance variations are believed to be mostly the result of active regions, which emit much more UV radiation than the quiet Sun. Short-term variations of UV at the Earth are mainly due to the evolution of active regions and the rotational modulation of active-region radiances.

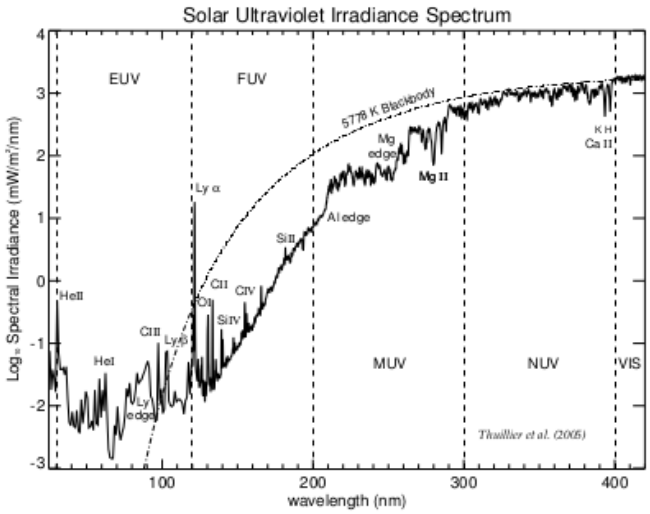

Fig 9. Solar ultraviolet spectrum. Adapted from [71]

During the flare events in October 2003, the observations made by the instruments aboard Solar Radiation and Climate Experiment (SORCE) spacecraft and the NASA Thermosphere, Ionosphere, Mesosphere, Energetics, and Dynamics (TIMED) spacecraft provided strong evidence for the increase in full-disk irradiance during large flares [73]. The high-cadence measurements showed an increase in TSI by 270 ppm during the X17 flare. The UV variations for this flare range from a factor of about 50 shortward of 10 nm to about 10% for the Mg II 280 nm emission. Further, broad wings of the H I Lyman-α (121.6 nm) emission increased by more than a factor of 2 during the flare while the core of the Lyman-α emission only increased by 20%. The Si III 120.6 nm emission also showed a sharp 1-minute long increase by a factor of 17

during the impulsive phase.

EUV radiation is highly energetic and gets easily absorbed in the Earth's upper atmosphere. It also ionizes the upper layer of the Earth's atmosphere, creating the ionosphere, thus its variability is directly linked to the variations in the ionosphere and upper atmosphere. EUV originates in the corona and chromosphere of the Suns atmosphere and is dominated by spectral lines from hydrogen, helium, oxygen, sodium, magnesium, silicon, and iron (as shown in Fig 9). Because solar EUV is absorbed by the upper atmosphere it is impossible to measure from the ground. Thus, measurements must be made above the Earth's atmosphere, e.g., rockets and satellites. There have been several space programs to measure UV radiation, however for long-term records, the proxies for solar EUV that can be measured from the ground, such as Sunspot Number or F10.7 cm radio flux, are used. At present time, space missions, such as NASA's TIMED/SEE, SORCE/EOS and SDO/EVE have been providing direct measurements of the UV variation for more than a decade.

Solar EUV has major impacts on communication and navigation. It modifies the total electron content (TEC), the total number of electrons present along a path between a transmitter and the receiver. During geomagnetic storms, there is a significant increase in the TEC due to the changes in the Earth's upper atmosphere in the presence of high EUV as waves propagate through the modified ionosphere. There are other local factors that may modify TEC, however geomagnetic storms have a severe impact. The more electrons in the path of the radio wave, the more the radio signal will be affected. The total delay suffered by a radio wave propagating through the ionosphere depends both on the frequency of the radio wave and the TEC. For ground to satellite communication and satellite navigation, TEC serves as a good parameter to monitor for possible space weather impacts. The NOAA/GOES satellite has been providing continuous measures of the electron flux since 1975.

2.6 Solar energetic particles

Solar energetic particles storms or solar radiation storms at Earth can occur throughout the solar cycle but are most frequent in solar maximum years [74]. However, enhanced radiation storms are observed when a large-scale magnetic eruption, often causing a coronal mass ejection and associated solar flare, accelerates charged particles in the solar atmosphere to very high velocities [75, 76]. Gopalswamy *et al* carried out a study of all the large solar energetic particle events that occurred during the minimum to maximum of solar cycle 23 [77]. With the limited number of samples, they concluded that the occurrence rate of the SEP events, and the fast and wide front-side western hemispheric CMEs is quite similar.This is consistent with the scenario that CME-driven shocks accelerate both protons and electrons; the SEP intensity is better correlated with the CME speed than with the X-ray flare class and CMEs associated with high-intensity SEPs are about 4 times more likely to be preceded by wide CMEs from the same solar source region.

The most important particles are protons which can get accelerated to one-third the speed of light. At these speeds, the protons can travel from the Sun to Earth in just 30 minutes. When they reach Earth, the fast moving protons penetrate the magnetosphere that shields Earth from lower energy charged particles and disturb the magnetic field lines. Solar radiation storm can persist for time periods ranging from hours to days. These storms cause several impacts near Earth. When energetic protons collide with any object/human in space, they can penetrate deep into the object and cause damage to electronic circuits or biological objects. Fig 10 shows the imprints of SEPs on the coronagraph images taken during the super storm in 2003. During these radiation storms, high flying aircraft at high latitudes may be exposed to radiation risk. When the energetic protons collide with the atmosphere, they ionize the atoms and molecules thus creating free electrons. These enhanced electrons counts can have an adverse effect on radio communication. Similar to X-ray and electron flux, SEPs have also been continuously measured by the NOAA/GOES satellite.

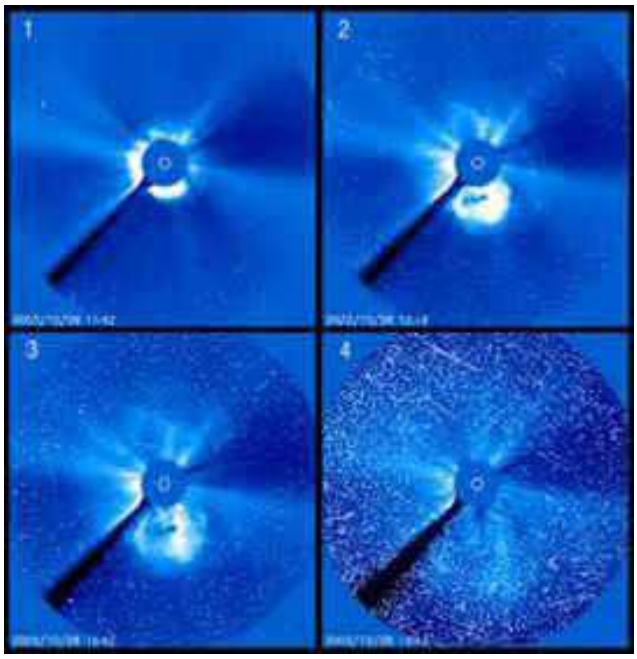

Fig 10. SOHO/LASCO coronagraph image capturing flare and resulting CME the from giant sunspot group 10486. In the bottom right frame, the coronagraph image is severely distorted by energetic particles.

3 Predicting space weather

Predicting solar magnetic activity is a valuable tool for the space weather forecasts. There are two kinds of predictions; one on the scale of solar cycle (see review by Tripathy [78] in this issue), and other on the scale of minutes to several days (will be discussed in this review). Accurate forecast depends largely on understanding the complex physical processes lying below and above the Sun's surface, and the interactions between Sun and Earth. Limited understanding of these processes is the major hindrance in space-weather predictions, however a large number of efforts in recent years have significantly advanced our knowledge. In particular, full-disk continuous solar observations from space and the ground at several wavelengths have played a major role in developing tools for forecasting. The synoptic vector magnetic-field measurements are playing a crucial role in the understanding of magnetic topology of space-weather source regions on the Sun, e.g. active regions, flares, chromospheric filaments, CMEs etc. In addition, helioseismology has demonstrated that many aspects of solar activity from flare and CME eruptions to cyclic variations may lie within the sub-photospheric plasma dynamics. Increased computation power and advanced modeling/ simulations have added new dimension to the space weather research and forecasting.

Below, we describe briefly the progress made in forecasting the solar sources that may lead to extreme space weather.

3.1 Emergence of active regions

Many physical processes are responsible for the formation of active regions, e.g. downflow of plasma along the rising flux tube, magnetic reconnection between the rising flux tubes and the ambient magnetic field lines etc. Observations suggest that the active regions form due to the emergence of several small flux tubes which are separted during the first phase of their appearance. With time, the flux tube clustering takes place until new magnetic field emerges from sub-photospheric layers. With the availability of high-resolution full

disk images at high cadence, there has been an upsurge in detecting the signatures of the emergence of active regions. Most of these attempts are based on identifying signatures in sub-surface layers using helioseismic methods on the front side as well as their existence on the farside of the Sun (the part that cannot be seen from the Earth's vantage point), which are highly dependent on analyzing the properties of localized regions. The important signatures that are used as precursors of the emergence are; the absorption of p-mode power as acoustic waves travel through the regions of high magnetic field [79], and the phase-shift produced by the scattering on p-modes by active regions [80] as described below:

3.1.1 Farside Active Regions

Detection of active regions on farside of the Sun's surface is based on the technique known as helioseismic holography, first described by Lindsey and Braun [81]. It is based on the fact that there is a phase shift or time delay between waves going in and out of an active region [79]. Hence, the waves that travel to the farside reflect back to the front side will carry information of the farside hemisphere. If any region with high magnetic fields encounters in their path, this information will be reflected in the phase-shift map. This technique was first applied to the full-disk MDI images where two big active regions were successfully detected before they turned towards the front side [82]. Details of this technique can be found in Lindsey and Brown [83]. It was further advanced by Gonzalez Hernandez *et al* [84] by converting phase-shift maps into the magnetic maps which proved to be instrumental in developing the routine farside active region monitoring system. At present, both GONG (*http://farside.nso.edu/*) and HMI (*http://jsoc.stanford.edu/ data/farside/*)

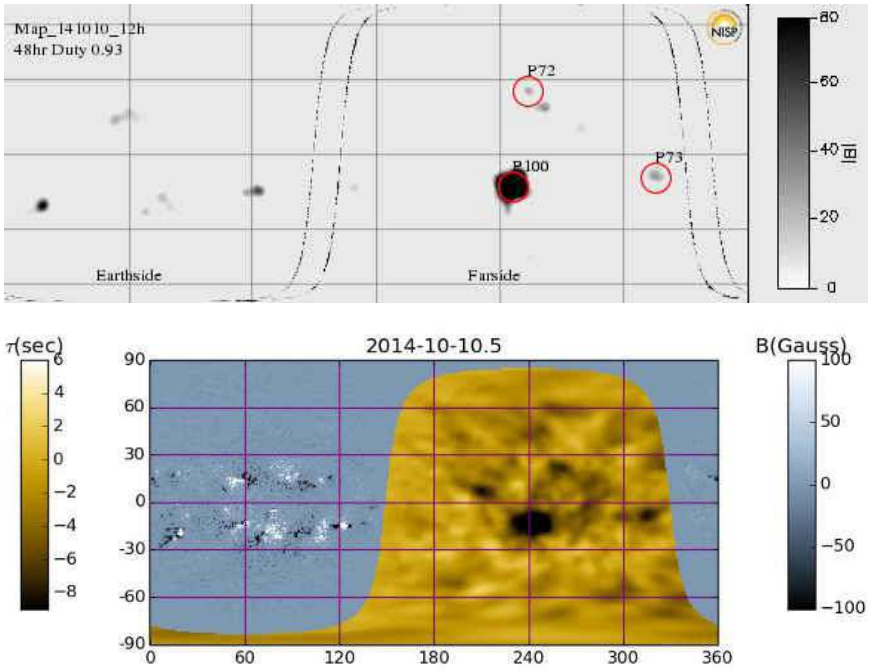

Fig 11. Simultaneous farside images of the Sun produced using full-disk images from (top) GONG (*http://farside.nso.edu/*) and (bottom) SDO/HMI (*http://jsoc.stanford.edu/data/farside/*). The dark region in the top image shows the existence of a big active region on the invisible surface. When this region turned towards Earth, it was given the NOAA number 12192. This is the biggest active region in the current solar cycle so far and lived for several rotations. The farside images were important to track it on the invisible side.

are producing these maps twice a day with key parameters such as location, phase shift/strength, probability, effective area, estimated arrival time at the solar east limb. To gain confidence in the prediction, farside maps

were compared with the backside images of the Sun from NASA's STEREO mission [85]. Approximately 90% of the helioseisimic active-region predictions matched the activity/brightness observed in EUV at the same locations. Fig 11 shows the sample farside maps from GONG and HMI when the AR 12192 is located on backside of the Sun. Both maps show a very strong signal supporting its existence. However, only the identification of these regions is not sufficient for space weather forecasting. Efforts are underway to identify the morphology of farside regions using the nearside helioseismic images [86].

3.1.2 Frontside active regions

While there are limited efforts for detecting farside active regions, the emergence of nearside region has been addressed in several studies. Most of these studies are based on the suppression in acoustic power, changes in subsurface wave-speed perturbations and plasma flows that serve as pre-cursors for the emergence of active regions. Some success was achieved in the detection of upward-moving magnetic structures, however the signatures of these structures could not be unambiguously established before the active region emergence in the photosphere. The fast emergence speed and the low signal-to-noise ratio of the helioseismic measurements at large depths also pose difficulties in the detection of pre-emergence signatures.

Most of these studies exploit the technique of time-distance helioseismology that images acoustic perturbations in the interior of the Sun [87]. Acoustic waves are excited by turbulent convection near the surface, propagate deep inside the Sun, and refract back to the surface. Time-distance method measures travel times of acoustic waves propagating to different distances by computing cross-covariances between the oscillation signals observed at pairs of locations on the solar photospheric surface. Variations in acoustic travel times are caused mainly by thermal perturbations, magnetic fields, and flows. Earlier studies of emerging sunspot regions have found it difficult to detect signals deeper than 30 Mm and before the initial magnetic field becomes visible on the surface because of the fast emergence speed and low signal-to-noise ratio [88]. In recent years, this method was further exploited by Ilonidis and co-workers, and a deep-focus time-distance measurement scheme was developed, which allows us to detect signals of emerging magnetic regions in the deep solar interior [89]. Strong acoustic travel-time anomalies of an order of 12 to 16 seconds were detected as deep as 65,000 kilometers. These anomalies were associated with magnetic structures that emerged with an average speed of 0.3 to 0.6 kilometer per second and caused high peaks in the photospheric magnetic flux rate 1 to 2 days after the detection of the anomalies. However, the observed phase-shifts prior to the emergence were large and difficult to reconcile with the current emerging flux models, hence this scheme received several criticisms. In an independent study using the same technique, these results have been partly confirmed by Kholikov [90]. As an example, in Fig 12, we show the travel-time maps for AR 10488. It can be seen that the travel times reached the maximum value several days before the emergence of the active region. Later, using the acoustic holography method, Braun could not confirm travel-time anomalies in four active region considered by Ilonidis and co-workers [91]. This method of predicting the emergence of active region needs more work and verification before it can be used for active region emergence monitoring.

Using numerical simulations, Hartlep *et al* studied the dependence of the acoustic power above a subsurface region on the sign, depth, and strength of the wave-speed perturbation [92]. They found the suppression in acoustic power in the frequency band of 3 - 4 mHz before the emergence, and successfully tested this methodology on the emergence of active region 10488. In a similar study, the acoustic power was measured by using phase-speed and ridge filters, and the signatures of rising motion of magnetic flux in the 10 – 15 Mm below the surface were detected. Recently, using the solar surface mode, i.e. the *f*-mode, it is shown that in the presence of a non-uniform magnetic field which is concentrated at a few scale heights below the surface, the *f*-mode fans out in the diagnostic $k\omega$ diagram at high wavenumbers [93]. These authors also tested this property on three active regions, i.e. NOAA 11768, 11158 and 12051, using the observations from SDO/HMI and showed that at large latitudinal wavenumbers (corresponding to horizontal scales of around 3000 km), the *f*-mode displays strengthening about two days prior to AR formation and thus provides a new precursor for active region formation.

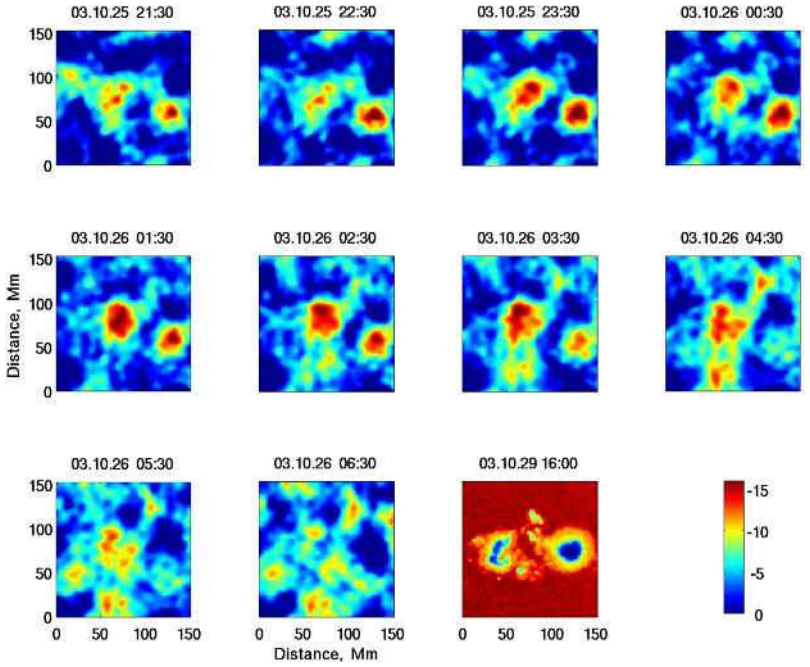

Fig 12. Deep focusing travel-time maps of the AR 10488 (top two rows and left two images in bottom row). The focus depth for these measurements covers 40 – 70 Mm. Each map is created using 8-hour duration MDI data cubes centered at the emerging active region location (dates and times are displayed at the top). The color scale in the travel-time maps covers the perturbation range 0 (blue) to −15 (red) seconds. The maximum time shift magnitude is observed at around 1:30 UT on 26 October. A continuum image for a later time is presented in the last panel of the bottom row. The active region location shows significant double structure travel-time perturbation on below the surface prior the emergence on 25 – 26 October, and after emergence on the surface on 29 October. (Adapted from Kholikov [90]).

In addition to several case studies on the emergence, attempts have also been made to understand statistically the properties of an ensemble of emerging and decaying flux regions. A series of studies with large samples of emerging-flux and quiet regions have been carried out by Komm *et al*. It was shown that emerging-flux regions are characterized by upflows [94], faster rotation [95], and increased vorticity of subsurface flows [96]. Using helioseismic holography, Birch *et al* reported evidence of statistically significant subsurface wave-speed perturbations and plasma flows at least a day before emergence [97]. In a subsequent study by the same group, best property for identifying the cases with emergence is found to be the surface magnetic field, even a day before the emergence time [98]. However, after accounting for the correlations between the surface field and the quantities derived from helioseismology as described in Ref. [97], some evidences of a helioseismic precursor to active region emergence, at least a day in advance, were also found. It should be noted, in contrast to the farside active region monitoring, such system for the emergence of these regions on the frontside is not yet established. It is believed that helioseismology may play a crucial role here, however a robust mechanism has yet to be identified.

3.2 Flares

Forecasting solar flares is a challenging subject. All major flares occur in complex sunspot groups, but it remains unclear how the probability of producing a flare of any given magnitude relates to the characteristics of the sunspot group. In general, methods with measured parameters from near-real

time active region photospheric field are used to calculate the probability of a particular flare to happen, however different methods provide different probabilities. The flare forecasting, at present, highly depends on various statistical methods. For example, Barnes *et al* applied the discriminant analysis to provide the probability of active regions for their flaring/non-flaring characteristics based on a set of variables relevant to the photospheric magnetic field derived from the vector magnetic field measurements [99]. While this is still a topic of research, there are several models/methods which are currently in use for operational flare forecasting.

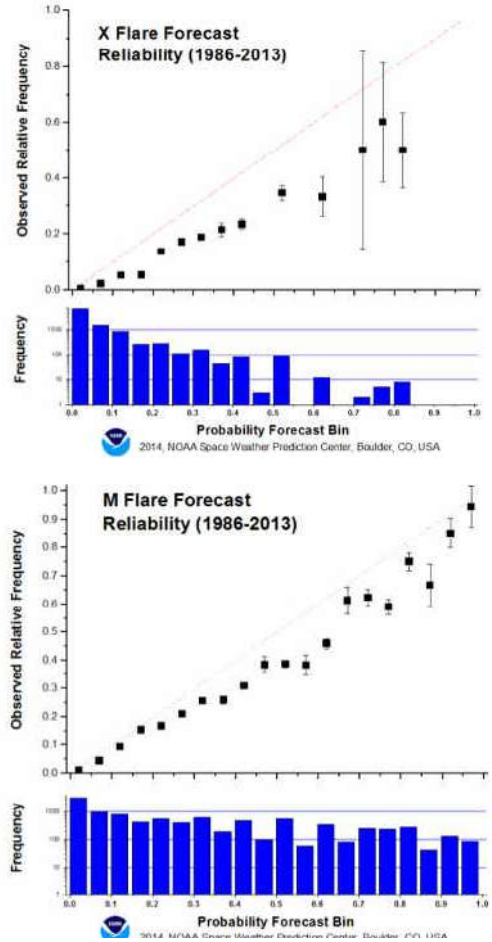

Fig 13. 1-day lead time X-class (top) and M-class flare forecast "reliability" during the period 1986 to 2013. In each box, the top panel plots the observed relative frequency of flare days (days on which an X or M flare occurred) against their corresponding forecasts, grouped in 5% (0.05) bins. The dashed diagonal line represents perfect correspondence. Points falling below or above the diagonal indicate a tendency of the forecasts within that bin to over-predict or under-predict the occurrence of flares in the respective category. Error bars correspond to the standard error associated with the number of forecasts in each bin and t he number of forecasts in each bin is plotted in the bottom panel histogram. Credit: NOAA/SWPC.

SWPC provides advance warning for any space weather event with adverse effects. Their flare forecast is based on look-up tables [100], which provide forecasts for each active region visible daily for 24-h, 48-h, and 72-h intervals (*ftp://ftp.swpc.noaa.gov/pub/forecasts/daypre/*). For this purpose, the key information

on each active region such as region classification (McIntosh class [101]), magnetic classification, spot count, areal coverage, location etc. are extracted from the daily images and provided to forecasters for assigning a probability based on the climatologically lookup tables. These lookup tables contain flare probability as a function of parameters mentioned above. The reliability of M- and X-class flare forecast during the period 1986-2013 is illustrated in Fig 13. While the SWPC prediction strategy needs human intervention, the models running at the NASA's Community Coordinated Modeling Center (*ccmc.gsfc.nasa.gov*) are fully automated (*http://iswa.ccmc.gsfc.nasa.gov/iswa data tree/model/solar/*).

The MAG4, a physics-based model, was developed by the University of Alabama team which uses the of transverse gradient of the line-of-sight magnetic field integrated over all polarity inversion lines present in the strong field areas as a proxy for active region free magnetic energy [102]. The output from this model is updated every hour (*http://iswa.ccmc.gsfc.nasa.gov/iswa_data _tree/model/solar/mag4/*). Recently, Guerra *et al* [103] presented test results on the ensemble forecasting of major solar flares by including probabilistic forecasts from three to four models, i.e. MAG4, ASAP (Automated Solar Activity Prediction developed by the University of Bradford Group in UK), ASSA (Automatic Solar Synoptic Analyzer developed at Korean Space Weather Station), and the NOAA/SWPC forecast. Details of the ASSA and ASAP models can be found at *http://www.spaceweather.go.kr/assa/* and in Colak and Qahwaji [104], respectively. In both models, the sunspot groups are identified and classified according the McIntosh style classification. In ASSA, the flare probabilities are calculated for each active region using Poisson statistics based on the average flare rates for its McIntosh class while ASAP uses the area of each sunspot group and its McIntosh class as input in two neutral-network systems that were trained using a catalog of solar flare events from 1982 to 2006. The results of ensemble forecasting based on linear combination are encouraging based on a small sample of active regions in Cycle 24. A large sample of flaring regions needs to be tested to gain confidence in ensemble forecasting.

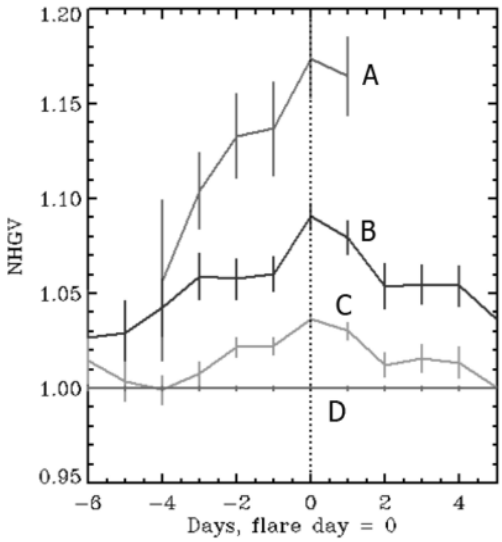

Fig 14. Superposed epoch analysis for active regions associated with X-class flares (A), M-class flares (B), C-class flares (C) while an average values for non-flaring active regions is shown by (D). (Adapted from Reinard *et al* [106])

In addition to photospheric magnetic features, the dynamical sub-surface parameters have also been used as predictors for flare production. Komm and Hill identified helicity and vorticity calculated from the sub-surface horizontal flows underneath active regions [105]. The statistical analysis of these derived

parameters associated with active regions hints that the kinetic helicity density decreases a few days prior to the flare eruption [106]. To represent the changes in helicity density, a parameter called Normalized Helicity Gradient variance (NHGV) was derived that captures the changes within a depth range of 0.6 and 15.8 Mm below the surface. As shown in Fig 14, this parameter significantly increases days before the flare occurs. This method was applied to various ensembles of active regions with different flaring properties. More work on a large sample of individual is needed to make it an operational tool.

3.3 CMEs, Solar wind and geomagnetic storms

Since interplanetary coronal mass ejections (ICMEs) are the main drivers of geomagnetic storms, forecasting their arrival time at Earth along with the direction and speed of the ejected material are crucial. These factors depend on the direction and speed of the solar wind, which is a persistent background stream of particles emitted by the Sun. There are several forecasting tools used for real-time modeling of the heliospheric propagation of ICMEs, ranging from simple empirical procedures to analytical models based on MHD and to sophisticated numerical models *(http://swrc.gsfc.nasa.gov/main/cmemodels*).

The WSA-ENLIL+Cone model is a numerical model that is widely used to predict CME arrival at the Earth [107]. This model was originally developed as ENLIL model to provide simulations of solar-wind conditions based on the inputs from synoptic photospheric magnetograms. Later, it was extended to incorporate a CME-like feature at the inner boundary of the ENLIL numerical mesh and tracks the propagation of the solar wind disturbance through the heliosphere. This extended model is now known as the WSA-ENLIL+Cone model, runs at *http://ccmc.gsfc.nasa.gov/*, and is routinely used to provide 1-4 day advance warning of solar wind structures and Earth-directed coronal mass ejections, such as velocity, density, and dynamic pressure (*http://www.swpc.noaa.gov/products/wsa-enlil-solar-wind-prediction*), see Fig 15. Input parameters to this model are the CME data from coronagraphic observations up to a radial-distance range of about 20 solar radii and rely on cone geometry of the CME.

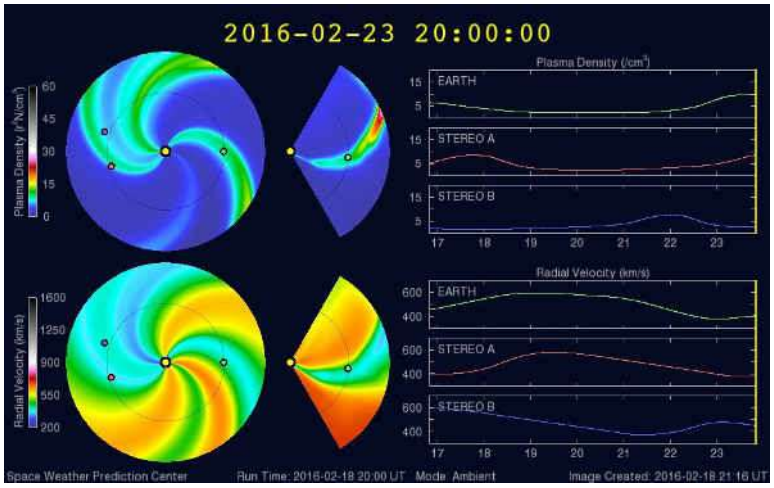

Fig 15. Forecast of the solar wind speed and density at the Earth and the positions of the two STEREO spacecraft. Courtesy: NOAA/SWPC.

The drag-based model (DBM) is an analytical model and basically describes the propagation of the front part of the ICME body, i.e., in its basic form it does not reproduce the propagation of the ICME-driven shock/sheath region. The DBM is based on the assumption that beyond a certain heliocentric distance, the ICME propagation is governed solely by its interaction with the ambient solar wind, i.e., acceleration/deceleration of the ICME can be expressed in terms of the MHD analog of aerodynamic drag [108]. It has

been shown that the arrival-time predictions from both WSA-ENLIL+Cone model and the drag-based model are comparable and provide forecast of CME arrival and impact speed at 1 AU with lead times of about 24 days [109]. This is also one of the registered methods at the Space Weather Score Board at CCMC (*http://kauai.ccmc.gsfc.nasa.gov/SWScoreBoard/*).

The Empirical Shock Arrival (ESA) model was developed by Gopalswamy *et al* [110] based on quadrature data from Helios (*in situ*) and P-78 (remote sensing) to predict the 1-AU arrival of coronal mass ejections. The ESA model requires earthward CME speed as input, which is not directly measurable from coronagraphs along the Sun-Earth line. Recently, they used quadrature observations from STEREO and SOHO to test the capability of ESA model for a set of 20 events [111] and found that the ESA model shock arrival predictions with the RMS error are comparable to the predictions from the WSA-ENLIL+Cone model.

3.4 Solar energetic particles

The forecasting of SEP events is primarily based on the estimates of magnetic free energy in active regions and on the observations of peak fluxes of M- and X-class flares. Due to the sporadic nature of these events and lack of complete understanding of the mechanisms (i.e. acceleration and propagation) involved in their generation, the forecasting is not trivial. However, it is well understood that the fast CMEs and SEP events are closely related to each other. There are several schemes of SEPs prediction; the empirical models rely on the observations of associated precursor phenomena and in the other category physics-based numerical models of particle injection, shock evolution and SEP acceleration at shocks are used. Below, we mention a few empirical models that are in use nowadays.

The Forecasting Solar Particle Events and Flares (FORSPEF) scheme provides nowcasting and forecasting of solar eruptive events, such as solar flares with a projection to CMEs (occurrence and velocity), likelihood of a SEP event as well as the complete SEP profile [112]. It is based on a purely statistical approach where for a given location of an active region, the information stored in the FORSPEF database is used to derive the distribution functions of the flare magnitudes associated and/or not associated with SEPs. The database is constructed on the basis of soft X-ray measurements from GOES and CME information from SoHO/LASCO, and cover an interval of 30 years. The forecasts are available up to 24 hours in advance and provide near real-time assessments (typically 15-20 minutes) of the near Earth environment. Another method, known as University of Malaga Solar Energetic Particle (UMASEP), predicts in real time the expected time interval on which the integral proton may reach the SEPs threshold of 10 MeV set by the SWPC [113]. It also predicts the intensity of the first few hours of SEP events.. The prediction capabilities of this model have been recently expanded to 100 MeV [114]. Another model, known as the proton prediction system (PPS), was developed to predict solar energetic ($E > 5$, 10, 50 MeV) intensities at 1 AU following solar flares. It is based on average observed SEP intensity-time profiles, peak intensities, and event durations. The input parameters are solar flare peak, time-integrated X-ray, radio fluxes and their times of onsets and maxima, and solar flare locations [115]. In addition, there are a few physics-based models however these are not yet mature for operation purposes.

3.5 Solar EUV irradiance

There are both empirical and physics-based approaches for the EUV modeling and forecasting. The empirical models, frequently known as proxy models, are derived from the linear relationships between a proxy of solar activity and the direct observations of the irradiance. The 10.7 cm radio flux, available since 1947, has been widely used to develop proxy models for the solar EUV variability. As an example, we show in Fig 16 the composite Lyman-α time series since 1947 constructed with the measurements from various instruments (whenever available) and the models for 10.7 cm radio flux (to fill in the gaps between measurements). In particular, Tobiska and his team at Space Environment Technologies (SET) have developed a series of proxy models SERF 2 [116], EUV91 [117], EUV97 [117] and SOLAR2000 [118]. Besides improving the accuracy

of previous models, the SOLAR2000 was also designed to provide accurate forecasts and specifications of the solar spectrum. A new proxy, E10.7, was proposed which is basically the time-dependent, integrated solar EUV at the top of the Earth's atmosphere and is reported in 10.7 cm radio units. This model/tool is in operation at SET and now known as Solar Irradiance Platform (SIP). This new tool produces the variable, full solar spectrum in assorted spectral formats for historical, nowcast, and forecast applications. In addition, it also produces an array of solar irradiance and thermospheric proxies. However, Viereck *et al* [119] argued that the Mg II index is the better proxy for EUV radiation than the F10.7 and now has been used in several models.

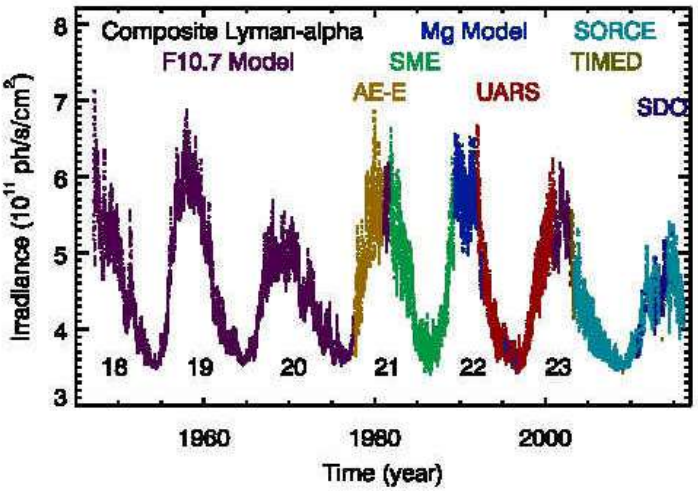

Fig 16. The composite Lyman-α time series includes measurements from multiple instruments and models (using 10.7 cm radio flux) to construct a long time series history of the bright solar H I 121.6 nm emission. Measurements are used whenever they are available. (Credit CU/LASP)

More recently, Henney *et al* [120] developed a method to forecast the F10.7 using advanced predictions of the global solar magnetic field generated by the AirForce Data Assimilative Photospheric Flux Transport (ADAPT) model. They first studied the correlation between observed magnetic field and F10.7, and found a good correlation between these two quantities. Then by evolving the solar magnetic synoptic maps forward 1-7 days with the ADAPT model, they estimated the Earth-side solar magnetic field distribution that was further used to forecast radio flux. This method was further refined by including calibrated farside helioseismic maps of the Sun from GONG as input to the ADAPT model [121] which improved the forecast. Later, same technique was applied to forecast the solar irradiance of selected wavelength ranges within the EUV and FUV bands [122]. It is suggested that the observed F10.7 signal correlates well with strong magnetic field (i.e., sunspot) regions while the EUV and FUV signals are significantly correlated with the weaker magnetic fields associated with plage regions. They argued that the solar magnetic indices may be used as an improved indicator (relative to the widely used F10.7 signal) of EUV and FUV non-flaring irradiance variability.

4 Summary

In summary, solar activity is the major driver of space weather. Its eurptive phenomena, such as flares, coronal mass ejections, may create conditions that can affect human and technology in many ways, some may lead to catastrophic effects. Thus, it is important to understand their origin, the complex physical processes lying below and above the Sun's surface, and the interactions between Sun and Earth. In order to minimize the adverse effects, there is a strong need to improve space weather forecasting capabilities. These

capabilities can be enhanced with modeling/simulations along with the observations. Although space weather forecasting is still several decades behind that of the terrestrial weather, there has been significant progress made in the last couple of decades — thanks to high-computing power and the continuous observations from both space and ground. This further requires timely planning of new missions. In recent years, space weather forecasters have realized the need of observing the Sun's activity from a different vantage point before the Sun turns towards the Earth. There have been efforts going on to view the solar disturbances and their solar sources from the L5 vantage point (e.g., [123]), however case studies are needed to bring them to reality. In this direction, the Carrington-L5 mission, a dedicated UK/US mission for space weather, is expected to give a five-day warning of hazardous solar activity [124]. The spacecraft is planned to fly to a point nearly 100 million miles behind the Earth, but in the same orbit around the Suna stable point known as L5. That will allow it to see activity on the Sun before it spins into view from Earth and by combining its observations with those from other satellites, it will give a 3D view of CMEs to show if any are heading our way. The current launch date of this mission is in 2021.

Acknowledgments

SDO data courtesy of SDO (NASA) and the HMI and AIA consortium. SOHO is a mission of NASA and ESA. This work utilizes GONG data obtained by the NSO Integrated Synoptic Program (NISP), managed by the National Solar Observatory, the Association of Universities for Research in Astronomy (AURA), Inc. under a cooperative agreement with the National Science Foundation. The data were acquired by instruments operated by the Big Bear Solar Observatory, High Altitude Observatory, Learmonth Solar Observatory, Udaipur Solar Observatory, Instituto de Astrofisica de Canarias, and Cerro Tololo Interamerican Observatory. We thank Shukur Kholikov for providing Fig 12.

References

1. Carrington R C, *Mon Not Royal Astron Soc*, 20(1859)13-15.
2. Tsurutani B T, Gonzalez W D, Lakhina G S, Alex S, *J Geophys Res*, 108(2003)1268.
3. Tsurutani B T, Judge D L, Guarnieri F L, Gangopadhyay P, Jones A R, Nuttall J, Zambon G A, Didkovsky L, Mannucci A J, Iijima B, Meier R R, Immel T J, Woods T N, Prasad S, Floyd L, Huba J, Solomon S C, Straus P, Viereck R, *Geophys Res Lett*, 32(2005)L03S09.
4. Schwenn R, *Liv Rev Sol Phys*, 3(2006)2.
5. Cliver E W, Svalgaard L, *Sol Phys*, 224(2004)407-422.
6. Veselovsky I S, Panasyuk M I, Avdyushin S I, Bazilevskaya G A, Belov A V, Bogachev S A, Bogod V M, Bogomolov A V, Bothmer V, Boyarchuk K A, Vashenyuk E V, Vlasov V I, Gnezdilov A A, Gorgutsa R V, Grechnev V V, Denisov Y I, Dmitriev A V, Dryer M, Yermolaev Y I, Eroshenko E A, Zherebtsov G A, Zhitnik I A, Zhukov A N, Zastenker G N, Zelenyi L M, Zeldovich M A, Ivanov-Kholodnyi G S, Ignat'ev A P, Ishkov V N, Kolomiytsev O P, Krasheninnikov I A, Kudela K, Kuzhevsky, B M, Kuzin, S V, Kuznetsov, V D, Kuznetsov, S N, Kurt, V G, Lazutin, L L, Leshchenko, L N, Litvak, M L, Logachev, Y I, Lawrence, G, Markeev, A K, Makhmutov, V S, Mitrofanov, A V, Mitrofanov, I G, Morozov, O V, Myagkova, I N, Nusinov, A A, Oparin, S N, Panasenco, O A, Pertsov, A A, Petrukovich, A A, Podorol'sky, A N, Romashets, E P, Svertilov, S I, Svidsky, P M, Svirzhevskaya, A K, Svirzhevsky, N S, Slemzin V A, Smith Z, Sobel'man I I, Sobolev D E, Stozhkov Y I, Suvorova A V, Sukhodrev N K, Tindo I P, Tokhchukova S K, Fomichev V V, Chashey I V, Chertok I M, Shishov V I, Yushkov B Y, Yakovchouk O S, Yanke V G, *Cosmic Res*, 42(2004)435-488.
7. Gopalswamy N, Yashiro S, Liu Y, Michalek G, Vourlidas A, Kaiser M L, Howard R A, *J Geophys Res*, 110 (2005)A12S07.
8. Dellinger J H A, *Science*, 82(1935)351.
9. Shibata K, Magara T, *Liv Rev Sol Phys*, 8(2011)6.
10. Webb D F, Howard T A, *Liv Rev Sol Phys*, 9(2012)3.
11. Kahler S W, *Ann Rev Astron Astrophys,* 30(1992)113-141.

12. Gosling J T, *J Geophys Res*, 98(1993)18937-18950.
13. Pulkkinen, T, *Liv Rev Sol Phys*, 4(2007)1.
14. American Meteorological Society Satellite Navigation Space Weather: Understanding the Vulnerability Building Resilience AMS, 2011 (https://www.ametsoc.org/ams/assets/File/spacWx_GPS_2010.pdf).
15. Lean J, *Rev Geophys*, 29(1991)505-535
16. Schrijver C J, Kauristie K, Aylward A D, Denardini C M, Gibson S E, Glover A, Gopalswamy N, Grande M, Hapgood M, Heynderickx D, Jakowski N, Kalegaev V V, Lapenta G, Linker J A, Liu S, Mandrini C H, Mann I R, Nagatsuma T, Nandy D, Obara T, Paul O'Brien T, Onsager T, Opgenoorth H J, Terkildsen M, Valladares C E, Vilmer N, *Adv Space Res*, 55(2015)2745-2807.
17. Gosain S, *Asian J Phys*, 25(2016)221-232.
18. Pesnell W D, *Asian J Phys*, 25(2016)233-265.
19. Kaiser M L, Kucera T A, Davila J M, St Cyr O C, Guhathakurta M, Christian E, *Space Sci Rev*, 136(2008) 5-16.
20. Pesnell W D, Thompson B J, Chamberlin P C, *Sol Phys*, 275(2012)3-15.
21. Veronig A M, Potzi W, in Ground-based Solar Observations in the Space Instrumentation Era, (eds) I Dorotovic, C E Fischer, M Temmer, *Astron Soc Pacific Conf Ser*, 504(2016)247-262
22. Roth M, Gosain S, Hill F, Thompson M, The Solar Physics Research Integrated Network Group, in 12th Eoropean Space Weather Week, 2015.
23. Arge C N, Pizzo V J, *J Geophys Res*, 105(2000)10465-10480.
24. Odstrcil D, Pizzo V J, Linker J A, Riley P, Lionello R, Mikic Z, *J Atmos Sol-Terres Phys*, 66 (2004)1311-1320.
25. Odstrcil D, Pizzo V J, Arge C N, *J Geophys Res – Space Res*, 110(2005)A02106.
26. Pizzo V, Millward G, Parsons A, Biesecker D, Hill S, Odstrcil D, *Space Weather*, 9(2011)03004.
27. Steenburgh R A, Biesecker D A, Millward G H, *Sol Phys*, 289(2014)675-690.
28. Ambastha A, *Asian J Phys*, 25(2016)267-294.
29. van Driel-Gesztelyi L, Green L M, *Liv Rev Sol Phys*, 12(2015)1.
30. Smith S F, Howard R, (ed) K O Kiepenheuer, *IAU Symposium*, 33(1968)33.
31. Bumba V, Howard R, *3.4 Magnetograms*, 7(1969)28-38.
32. Gaizauskas V, Harvey K L, Harvey J W, Zwaan C, *Astrophys J*, 26(1983)1056-1065.
33. Harvey K L, Zwaan C, *3.4 Magnetograms*, 148(1993)85-118.
34. Schmieder B, Démoulin P, Pariat E, Török T, Molodij G, Mandrini C H, Dasso S, Chandra R, Uddin W, Kumar P, Manoharan P K, Venkatakrishnan P, Srivastava N, *Adv Space Res*, 47(2011)2081-2091.
35. Bai T, *Astrophys J*, 314(1987)795-807.
36. Bai T, *Astrophys J Lett*s, 364(1990)L17-L20.
37. Archontis V, Tsinganos K, Gontikakis C, *Astron Astrophys*, 512(2010)L2.
38. Gyenge N, Ludmány A, Baranyi T, *Astrophys J*, 818(2016)127.
39. Sun X, Bobra M G, Hoeksema J T, Liu Y, Li Y, Shen C, Couvidat S, Norton A A, Fisher G H, *Astrophys J Lett*, 804(2015)L28.
40. Evershed J, *MNRAS,* 69(1909)454-457.
41. Brown D S, Nightingale R W, Alexander D, Schrijver C J, Metcalf T R, Shine R A, Title A M, Wolfson, *Sol Phys,* 216(2003)79-108.
42. Stenflo J O, *Sol Phys*, 8(1969)115-118.
43. Yan X -L, Qu Z -Q, Kong D -F, *Mon Not Royal Astron Soc*, 391(2008)1887-1892.
44. Zhang, Y, Liu, J, Zhang H, *Sol Phys*, 247(2008)39-52.
45. Moffatt H K, *Magnetic field generation in electrically conducting fluids*, (Cambridge University Press), 1978.
46. Berger M A, Field G B, *J Fluid Mech*, 147(1984)133-148.
47. Bao S, Zhang H, *Astrophys J Lett*, 496(1998)L43-L46.
48. Hagino M, Sakurai T, *Pub Astron Soc Jpn*, 57(2005)481-485.

49. Pevtsov A A, Canfield R C, Metcalf T R, *Astrophys J Lett*, 425(1994)L117-L119.
50. Pevtsov A A, Canfield R C, Metcalf T R, *Astrophys J Lett*, 440(1995)L109-L112.
51. Moffatt H K, Tsinober A, *Ann Rev Fluid Mech*, 2(1992)281-312.
52. Benz A O, *Liv Rev Sol Phys*, 5(2008)1.
53. Low B C, *3.4 Magnetograms*, 167(1996)217-265. Pl check
54. Michalek G, Yashiro S, *Adv Space Res*, 52(2013)521-527.
55. Lavraud B, Rouillard A, in Nature of Prominences their Role in Space Weather, (eds) B Schmieder, J-M Malherbe, S T Wu, *Proc IAU Symposium*, 300(2013)273-284.
56. Srivastava N, Venkatakrishnan P, *Geophys Res Lett*, 29(2002)1287.
57. Michalek G, Gopalswamy N, Yashiro S A, *Astrophys J*, 584(2003)472-478.
58. Kim R -S, Cho K -S, Kim K -H, Park Y -D, Moon Y -J, Yi Y, Lee J, Wang H, Song H, Dryer M, *Astrophys J Lett*, 677(2008)1378-1384.
59. Gopalswamy N, Yashiro S, Michalek G, Xie H, Mäkelä P, Vourlidas A, Howard R A, *Sun Geosphere*. 5(2010) 7-16.
60. Vourlidas A, Bemporad A A, (eds) J Heerikhuisen, G Li, N Pogorelov, G Zank, *American Inst Phys Conf Ser*, 1436(2012)279-284.
61. Gonzalez W D, Tsurutani B T, Claude Gonzalez A L, *Space Sci Rev*, 88(1999)529-562.
62. Richardson I G, von Rosenvinge T T, Cane H V, *Sol Phys*, 290(2015)1741-1759.
63. Gopalswamy N, Yashiro S, Krucker S, Howard R A, (eds) K Dere, J Wang, Y Yan, *IAU Symp*, 226(2005)367-373
64. Michalek G, Gopalswamy N, Lara A, Yashiro S, *Space Weather*, 4 (2006)S10003.
65. Gopalswamy N, Yashiro S, Akiyama S, *J Geophys Res - Space Phys*, 112(2007)A06112.
66. Cranmer S R, *Liv Rev Sol Phys,* 6(2009)3.
67. He J -S, Tu C -Y, Tian H, Marsch E, *Adv Space Res*, 45(2010)303-309.
68. Zhao L, Landi E, *Astrophys J*, 781(2014)110.
69. Aschwanden M J, *Physics of the Solar Corona- An Introduction,* (Praxis Publishing Ltd), 2004.
70. Stone E C, Frandsen A M, Mewaldt R A, Christian E R, Margolies D, Ormes J F, Snow, F, *Space Sci Rev*, 86 (1998)1-22.
71. Thuillier G Floyd L Woods T N, Cebula R, Hilsenrath E, Hersé M, Labs D, *Adv Space Res*, 34(2004)256-261.
72. Fröhlich C, Lean J, *Astron Astrophys Rev*, 12(2004)273-320.
73. Woods T N, Eparvier F G, Fontenla J, Harder J, Kopp G, McClintock W E, Rottman G, Smiley B, Snow M, *Geophys Res Lett*, 31(2004)L10802.
74. Gabriel S B, Patrick G J, *Space Sci Rev*, 107(2003)55-62.
75. Kozarev K A, Raymond J C, Lobzin, V V, Hammer M, *Astrophys J*, 799(2015)167.
76. Klecker B, *J Phys Conf Ser*, 409(2013)012015.
77. Gopalswamy N, Yashiro S, Lara A, Kaiser M L, Thompson B J, Gallagher P T, Howard R A, *Geophys Res Lett*, 30(2003)8015.
78. Tripathy S C, *Asian J Phys*, 25 (2016)387-410.
79. Braun D C, Labonte B J, Duvall T L (Jr), *Astrophys J*, 354(1990)372-381.
80. Braun D C, Duvall T L (Jr), Labonte B J, Jefferies S M, Harvey J W, Pomerantz, M A, *Astrophys J Lett*, 391 (1992)L113-L116.
81. Lindsey C, Braun D C, *3.4 Magnetograms*, 126(1990)101-115.
82. Lindsey C, Braun D C, *Science*, 287(2000)1799-1801.
83. Lindsey C, Braun D C, *3.4 Magnetograms*, 192(2000)261-284.
84. González Hernández I, Hill F, Lindsey C, *Astrophys J*, 669(2007)1382-1389.
85. Liewer P C, González Hernández I, Hall J R, Lindsey C, Lin X, *3.4 Magnetograms*, 289 (2014)3617-3640.
86. MacDonald G A, Henney C J, Díaz Alfaro M, González Hernández, I, Arge C N, *Astrophys J*, 807(2015)21.

87. Duvall T L (Jr), Jefferies S M, Harvey J W, Pomerantz M A, *Nature*, 362(1993)430-432.
88. Jensen J M, Duvall T L (Jr), Jacobsen B H, Christensen-Dalsgaard J, *Astrophys J Lett*, 553(2001)L193-L196.
89. Ilonidis S, Zhao J, Kosovichev A, *Science*, 333(2011)993-996.
90. Kholikov S, *Sol Phys*, 287(2013)229-237.
91. Braun D C, *Sol Phys*, 289(2014)459-474.
92. Hartlep T, Kosovichev A G, Zhao J, Mansour N N, *Sol Phys*, 268(2011)321-327.
93. Singh N K, Raichur H, Brandenburg A, http://adsabs.harvard.edu/abs/2016arXiv160100629S.
94. Komm R, Howe R, Hill F, *Sol Phys,* 258 (2009)13-30.
95. Komm R, Howe R, Hill F, *Sol Phys*, 268 (2011)407-428.
96. Komm R, Howe R, Hill F, *Sol Phys*, 277(2012)205-226.
97. Birch A C, Braun D C, Leka K D, Barnes G, Javornik B, *Astrophys J*, 762(2013)131.
98. Barnes G, Birch A C, Leka K D, Braun D C, *Astrophys J*, 786 (201419.
99. Barnes G, Leka K D, Schumer E A, Della-Rose D J, *Space Weather*, 5(2007)S09002.
100. Crown M D, *Space Weather*, 10 (2012)S06006.
101. McIntosh P S, *Sol Phys*, 125(1990)251-267.
102. Falconer D A, Moore R L, Barghouty A F, Khazanov I, *Space Weather*, 12(2014)306-317.
103. Guerra J A, Pulkkinen A, Uritsky V M, *Space Weather*, 13(2015)626-642.
104. Colak T, Qahwaji R, *Space Weather*, 7(2009)S06001.
105. Komm R, Hill, F, *Journal of Geophysical Research* (Space Physics), 114(2009)A06105.
106. Reinard A A, Henthorn J, Komm R, Hill F, *Astrophys J Lett*, 710(2010)L121-L125.
107. Odstrčil D, Pizzo, V J, *J Geophys Res*,104(1999)28225-28240.
108. Vršnak B, Temmer M, Žic T, Taktakishvili A, Dumbović M, Möstl C, Veronig A M, Mays M L, Odstrčil D, *Astrophys J* Suppl, 213(2014)21.
109. Vršnak B, Žic T, Falkenberg T V, Möstl C, Vennerstrom S, Vrbanec D, Astron Astrophys, 512(2010)A43.
110. Gopalswamy N, Lara A, Yashiro S, Kaiser M L, Howard R A, *J Geophys Res*, 106(2001)29207-29218.
111. Gopalswamy N, Mäkelä P, Xie H, Yashiro S, *Space Weather*, 11(2013)661-669.
112. Papaioannou A, Anastasiadis A, Sandberg I, Georgoulis M K, Tsiropoula G, Tziotziou K, Jiggens P, Hilgers A A, *J Phys Conf Ser*, 632(2015)012075.
113. Núñez, M, *Space Weather*, 9(2011)07003.
114. Núñez, M, *Space Weather*, 13(2015)807-819.
115. Kahler S W, Cliver E W, Ling A G, *J Atmos Sol-Terres Phys*, 69(2007)43-49.
116. Tobiska W K, Barth C A, *J Geophys Res*, 95(1990)8243-8251.
117. Tobiska W K, *J Atmos Terres Phys*, 53(1991)1005-1018.
118. Tobiska W K, Woods T, Eparvier F, Viereck R, Floyd L, Bouwer D, Rottman G, White O R, *J Atmos Sol-Terres Phys*, 62(2000)1233-1250.
119. Viereck R, Puga L, McMullin D, Judge D, Weber M, Tobiska W K, *Geophys Res Lett*, 28(2001)1343-1346.
120. Henney C J, Toussaint W A, White S M, Arge C N, *Space Weather*, 10(2012)S02011.
121. Arge C N, Henney C J, Hernandez I G, Toussaint W A, Koller J, Godinez H C Modeling, eds. G P Zank, J Borovsky, R Bruno, J Cirtain, S Cranmer, H Elliott, J Giacalone, W Gonzalez, G Li, E Marsch, E Moebius, N Pogorelov, J Spann, O Verkhoglyadova, *American Inst Phys Conf Ser*, 1539(2013)11-14.
122. Henney C J, Hock R A, Schooley A K, Toussaint W A, White S M, Arge C N, *Space Weather*, 13(2015)141-153.
123. Gopalswamy N, Davila J M, St Cyr O C, Sittler E C, Auchère F, Duvall T L, Hoeksema J T, Maksimovic M, MacDowall R J, Szabo A, Collier M R, *J Atmos Sol-Terres Phys*, 73(2011)658-663.
124. Trichas M, Gibbs M, Harrison R, Green L, Eastwood J, Bentley B, Bisi M, Bogdanova Y, Davies J, D'Arrigo P, Eyles C, Fazakerley A, Hapgood M, Jackson D, Kataria D, Monchieri E, Windred P, *Hipparchos*, 2(2015)25-31.

[*Received*:17.3.2016; *accepted*: 12.4.2016]